High-Performance Bimodal Evanescent-Field Sensor with Coherent Phase Readout

Antonia Torres-Cubillo, José Manuel Luque-González, Alejandro Sánchez-Postigo, Adrián Fernández-Gavela, J. Gonzalo Wangüemert-Pérez, Íñigo Molina-Fernández and Robert Halir

***Abstract*—By comparing optical signals travelling through a sensing and a reference arm, interferometric photonic sensors achieve remarkable sensitivities and detection limits using simple single-wavelength laser sources. Sensors based on bimodal waveguides can, in principle, provide the same advantages without requiring a reference arm, by comparing the propagation of two modes travelling through a single sensing waveguide. However, typical implementations of bimodal sensors face two challenges: (i) the abrupt mode excitation and recombination at the sensor input and output is inefficient, unbalanced in power and produces spurious reflections that can mask small sensing signals, (ii) the sinusoidal nature of the output signal can lead to ambiguities in the readout. Here we present a spiralled bimodal refractive index sensor with full mode conversion, multiplexing and demultiplexing and a coherent phase detection, providing an unambiguous linear phase readout with a compact and robust layout. Our sensors have been designed for a 1550 nm central wavelength, fabricated on a silicon nitride platform and validated with bulk sensing experiments, achieving a limit of detection of $\mathbf{1.67 \cdot 10^{-7}}$ RIU.**

***Index Terms*—Silicon photonics, refractive index sensor, bimodal interferometer, mode converter and multiplexer, coherent readout.**

I. Introduction

Photonic integrated sensors have been the subject of extensive research over the past decade, as they can be employed to perform quantitative, real-time, and label-free analysis of molecules both in the liquid an the gas phase, achieving an outstanding sensitivity with a reduced footprint [1]. Indeed, such sensors have been employed for the detection of disease biomarkers enabling early medical diagnosis [2], or for the accurate measurement of hazardous and greenhouse-effect gasses [3], which is of great importance in environmental and industrial applications. Moreover, sensors designed for silicon photonic platforms can be produced at large scale in well established semiconductor foundries and are amenable to integration with CMOS microelectronics, paving the way towards high-performance, compact lab-on-a-chip devices [4]. Photonic sensing systems operating in the near-infrared wavelength range can furthermore benefit from the low-cost and high-quality laser sources and detectors developed for telecom applications.

Most integrated sensor configurations can be categorized either as resonant or interferometric. Resonant sensors such as ring resonators offer dense integration due to their compact size [5], [6]. However, they require a tunable laser source, thus increasing the system complexity and cost. Sensors based on interferometers are particularly interesting due to their high sensitivity and low limits of detection while operating at a fixed wavelength [7], [8]. Indeed, Mach-Zehnder interferometers (MZI) have been extensively studied for the quantitative detection of biological analytes [9], [10]. In this configuration the sensing arm is exposed to the sample, whereas the reference arm is isolated from it. This need for two different physical optical paths increases the sensor's footprint. Bimodal interferometers (BI) provide an interesting alternative [11], [12]. As illustrated schematically in Fig. 1(a), in these sensors two orthogonal modes of a single multimode waveguide are excited. Changes in the refractive index of the sample affect these modes differently, so that, albeit both modes travel through a common path, they experience different phase shifts. As a consecuence, upon recombination, they create an interferogram at the output. This common path configuration can furthermore mitigate drifts associated with thermal fluctuations.

The performance of these sensors is substantially dependent on the balanced excitation and the controlled recombination of the two modes, which affects the contrast of the interferogram, and the ability to generate a linear output from the sinusoidal interferometric signal [13]. Conventional modal excitation and recombination relies on abrupt transitions between single-mode and multimode waveguides [14]–[16], see Fig. 1(a). These abrupt transitions are prone to reflections that can produce a Fabry-Pérot-like ripple masking small sensing signals. More sophisticated approaches, such as mode converters based on grating couplers, enabling full control over the modal power distribution [17], or on mode filtering with directional couplers [18], have also been proposed. To avoid ambiguity in the readout, modulation techniques combined with algorithms based on Fourier Series deconvolution or trigonometric properties can be used to obtain a linear readout at the expense of system simplicity and computational load [14], [19]. Phase-generated carrier (PGC) techniques have also been employed for univocal readout in MZI-based biosensors, using only two photodetectors, but require adding heaters to

Antonia Torres-Cubillo, José Manuel Luque-González, J. Gonzalo Wangüemert-Pérez, Íñigo Molina-Fernández and Robert Halir are with the Telecommunication Research Institute (TELMA) of the University of Malaga, 29010 Malaga, Spain.

J. Gonzalo Wangüemert-Pérez, Íñigo Molina-Fernández and Robert Halir are also with IBIMA-BIONAND, Málaga Tech Park, 29590 Malaga, Spain.

Alejandro Sánchez-Postigo was with the Telecommunication Research Institute (TELMA) of the University of Malaga while this work was developed and is currently with the Department for Quantum Technology of the University of Münster, 48149 Münster, Germany.

Adrián Fernández-Gavela is with the Department of Physics of the University of Oviedo, 33007 Oviedo, Spain.

Corresponding author: Antonia Torres-Cubillo (e-mail: atc@ic.uma.es).

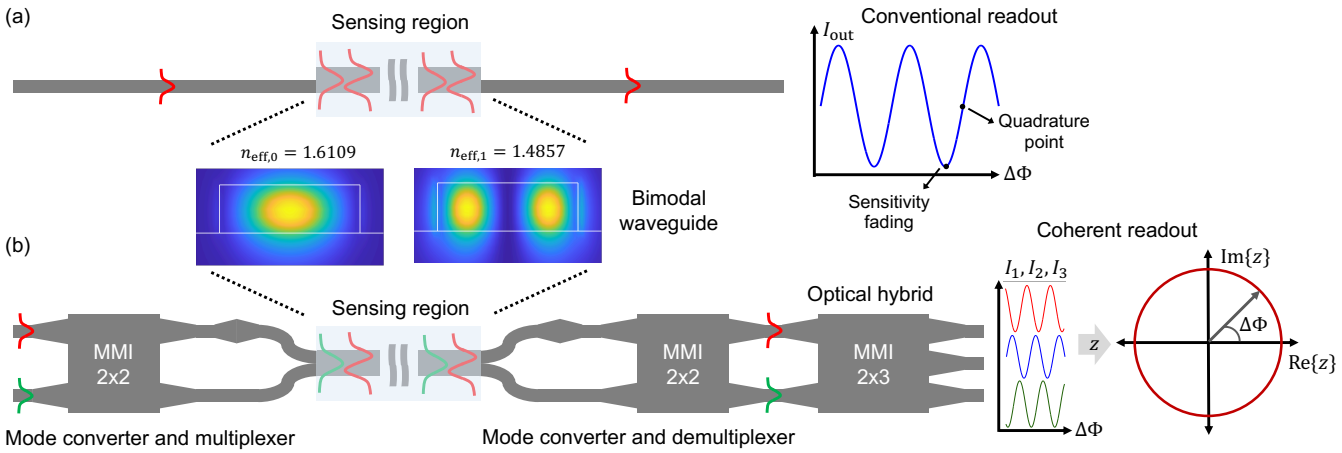

Fig. 1. Schematics of conventional and full-multiplexed coherent bimodal evanescent-field sensors. In both approaches the first two waveguide modes interact with the sample in a sensing window etched into the cladding, thereby accumulating a differential phase shift . (a) In the conventional architecture the two sensing modes are excited by an abrupt transition from a single-mode to a multimode waveguide. After propagation through the sensing waveguide, they are recombined via a second abrupt transition, yielding a single output intensity signal I_{out}( ). (b) In our architecture, two sensing modes are excited by a mode converter and multiplexer, and demultiplexed again after passing through the sensing region. This enables us to recombine them in a 2 3 MMI for full coherent phase retrieval.

the chip in order to perform an external phase modulation [20]. Modal demultiplexing combined with coherent detection aided by an optical hybrid has the potential to provide both low-loss excitation and splitting of the sensing modes and inherently linear phase readout [21], [22]. To the best of our knowledge, this approach has not yet been demonstrated with sensing experiments. Finally, with few exceptions [13], bimodal sensors make use of straight multimode waveguides, thereby hampering dense integration.

In this work, we experimentally demonstrate, for the first time, a silicon nitride bimodal sensor which combines balanced modal excitation and full mode demultiplexation with a coherent detection scheme facilitated by a 120 hybrid [see Fig. 1(b)]. Thanks to a spiralled two-mode waveguide, the sensor is remarkably compact, while achieving a state-of-the-art limit of detection (LOD). Moreover, our designs show robustness against fabrication tolerances.

The paper is organized as follows. In section II, the fundamentals of bimodal sensing, full mode demultiplexing and coherent readout are reviewed. Our designs are detailed in section III, with an emphasis on the mode converter and demultiplexer and the bimodal sensing waveguide. The results obtained after experimental validation are given in section IV. Finally, in section V, conclusions are drawn.

II. Fundamentals

A. Principles of bimodal sensing

Fig. 1(a) shows a schematic representation of a conventional bimodal evanescent-field sensor. Light travels in a single mode waveguide towards the sensing region, where it excites the sensing modes via an abrupt transition to a wider (or thicker) multimode waveguide. The liquid sample flows through a microfluidic channel placed on top of the sensing region, where the top cladding has been removed to enable interaction with the evanescent field of the two sensing modes. A change in the concentration of an analyte in the sample induces a change in its refractive index, Δn_{c}, which is translated into a change of the effective index of each of the guided modes, $\Delta n_{\text{e},0}$ and $\Delta n_{\text{e},1}$. The fundamental mode of the bimodal waveguide is more confined in the waveguide than the first high-order mode, and so its effective index changes at a smaller rate for a given change in the refractive index of the sample. Due to this differential change in effective index, after propagating a distance L through the waveguide, the two modes have accumulated a relative phase shift

$$\Delta\Phi = \frac{2\pi}{\lambda} L \left(\frac{\partial n_{\text{e},1}}{\partial n_{\text{c}}} \quad \frac{\partial n_{\text{e},0}}{\partial n_{\text{c}}} \right) \Delta n_{\text{c}}, \tag{1}$$

where λ is the free-space wavelength. Henceforth we will refer to $S_{\text{d}} = \partial n_{\text{e},1}/\partial n_{\text{c}} \quad \partial n_{\text{e},0}/\partial n_{\text{c}}$ as the differential mode sensitivity and to $S_{\text{bulk}} = \Delta\Phi/\Delta n_{\text{c}} = (2\pi/\lambda) S_{\text{d}} L$ as the overall sensitivity, expressed in radians (rad) per refractive index unit (RIU). Upon recombination in the output waveguide and detection via a photodiode, an intensity signal I_{out} / $\cos(\Delta\Phi)$ is obtained [11], [12], [23]. However, due to the cosenoidal nature of this signal the overall sensitivity is only achieved at the quadrature point, while it completely fades at the maxima and minima of the output intensity [see Fig. 1(a)]. Furthermore, the symmetric nature of the cosenoidal function leads to directional ambiguity, i.e. positive and negative phase changes cannot be distinguished.

B. Advantages of full mode demultiplexing

Multiplexing and demultiplexing of the guided modes, shown schematically in Fig. 1(b), provides a low-loss excitation of the first two TE modes and, after their propagation through the bimodal waveguides, splits them into the fundamental modes of two separate single-mode waveguides. These operations can be performed with negligible back reflections by using a simple and well-demonstrated mode converter and

(de)multiplexer topology [24], [25], which furthermore enables the use of advanced detection approaches developed for Mach-Zehnder interferometers. Specifically, by feeding the output fundamental modes into a 2 3 multimode interferometer (MMI) we can achieve a fully linear phase readout via coherent detection [22]. The 2 3 MMI delivers three interferometric output signals with a 120 phase shift between them. These three outputs are independently detected and combined by a coefficients matrix to generate a complex signal z / e^{j} . As a result, we obtain a linear and unambiguous output signal which can be directly correlated to the concentration of analyte in the sample, avoiding both sensitivity fading and directional ambiguity. Moreover, deterministic readout errors due to hardware non-idealities can be corrected by simple calibration algorithms [22], [26], contributing to relaxed fabrication tolerances.

III. Sensor Design

We designed our sensors for the commercial silicon nitride platform provided by Cornerstone [27], which offers a 300 nm Si_3N_4 device layer, a 3 m BOX layer and a 2 m silicon dioxide cladding, which is removed from the sensing area to enable the interaction of light with the sample. All our structures are manufactured via deep-ultraviolet projection lithography and a single step of reactive ion etching, ensuring cost-effective and scalable fabrication. Light coupling to and from the chip is performed via surface grating couplers. The central wavelength is $\lambda = 1550\,\mathrm{nm}$ and the polarization is TE. Electromagnetic simulations were carried out with RSoft Photonic Device Tools (Synopsys) [28].

A. Mode converter and multiplexer

The mode converter and multiplexer is shown schematically in Fig. 2(a) and is based on three elements: a 2 2-90 MMI, a 90 phase shifter and a symmetric Y-junction [24], [25]. A fundamental mode travelling through an interconnection waveguide with a width $W_{\mathsf{I}} = 0.9$ m is launched into the lower input port of the MMI and converted into the fundamental mode of the output waveguide, whereas the fundamental mode at the upper port of the MMI becomes the first high-order mode. This behavior arises as a combination of the 90 phase shift introduced by the MMI in the cross port, and the 90 phase shifter in the upper output. When operated in the opposite direction, the same structure performs the demultiplexation of the modes [Fig. 2(a)]. The figures of merit of the device are insertion loss (IL) and mode crosstalk (XT). Insertion loss is defined as the ratio of power in the desired mode in the multimode waveguide and the input mode: $\mathrm{IL}_{\mathsf{k}} = 10\log(P_k/P_{\mathsf{in}})$, $k = \{0, 1\}$; here the subscripts $0, 1$ refer to the fundamental and first high-order mode of the output waveguide, respectively. Crosstalk is defined as the power ratio between the undesired and the desired mode in the multimode waveguide: $\mathrm{XT}_{\mathsf{k}} = 10\log(P_k/P_j)$, $j, k = \{0, 1\}$, $j \neq k$. The MMI design is based on optimizing the width of the access waveguides (W_{a}) and the separation between them (s), to achieve a smooth transition between the access ports and the multimode region while suppressing

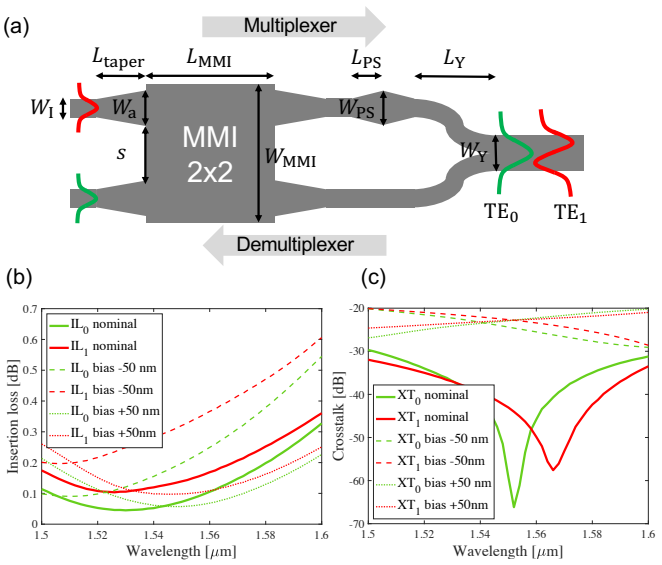

Fig. 2. (a) Schematic of the mode converter and (de)multiplexer used in this work. The input modes are converted into the fundamental and first high-order modes of the output waveguide respectively. b) 3D-FDTD simulated insertion loss of the input modes for the nominal design dimensions and 50 nm fabrication error. c) 3D-FDTD simulated mode crosstalk for the nominal design dimensions and 50 nm fabrication error.

power transfer between adjacent ports [see Fig. 2(a)]. The length of the taper (L_{taper}) is chosen large enough to ensure a virtually lossless transition. The width W_{MMI} and length L_{MMI} of the multimode region are designed to obtain the 3 dB splitting [29]. The phase shifter is designed by tapering one of the output ports of the MMI in back-to-back configuration, increasing the width to W_{PS} within a length L_{PS}. By doing so, a 90-degree phase shift compared with the straight waveguide in the bottom port of the MMI is accumulated [24]. Finally, a sinusoidal-profile Y-branch adiabatically combines the output waveguides of the phase shifter into the multimode waveguide over a length L_{Y}. This multimode waveguide is $W_{\mathsf{Y}} = 2W_{\mathsf{I}}$ wide, thus supporting thus supporting two TE modes. Figures 2(b) and 2(c) show the 3D-FDTD calculated performance for the geometric parameters included in Table I. The low loss ($< 0.5\,\mathrm{dB}$) and crosstalk ($< 30\,\mathrm{dB}$) of the structure allows for an efficient mode conversion and (de)multiplexing. The same structure has been simulated with a 50 nm fabrication bias error and the simulated insertion loss and crosstalk remain

TABLE I
GEOMETRIC PARAMETERS OF THE MODE CONVERTER AND MULTIPLEXER.

Component	Parameter	Value	Unit
MMI	W_{MMI}	7.4	µm
	L_{MMI}	167	µm
	s	1.5	µm
	W_{a}	3	µm
	L_{taper}	40	µm
Phase shifter	W_{PS}	1.1	µm
	L_{PS}	13.25	µm
Y-Branch	W_{Y}	1.8	µm
	L_{Y}	30	µm

well below $0.5\,\mathrm{dB}$ and below $20\,\mathrm{dB}$ respectively around the $1550\,\mathrm{nm}$ operating wavelength, as shown in Fig. 2(b-c). This ensures robustness against typical fabrication errors. As the sensing region is embedded between two mode demultiplexers [see Fig. 1(b)], the power reflected back by the structure is calculated to determine if a Fabry-Pérot cavity is created. 3D-FDTD simulations predict back reflections lower than $30\,\mathrm{dB}$ for both modes even in the presence of the fabrication bias mentioned above. Any Fabry-Pérot ripple is thus expected to be negligible.

B. Spiralled bimodal sensing waveguide

The bimodal waveguide is twice as wide as the single-mode interconnecting waveguide, i.e. $1.8\ \mathrm{m}$, and so it supports the first two TE modes. The electric field distributions of each mode are shown in Fig. 1. To evaluate the differential sensitivity (S_d), the change in the effective index of the guided modes was calculated as a function of the change in the refractive index of the cladding around a value of $1.32\,\mathrm{RIU}$, which corresponds to pure water at the design wavelength. The first high-order TE_{10} mode is significantly less confined in the waveguide than the fundamental TE_{00} mode and is thus more sensitive to changes in the cladding refractive index. We obtained a differential bulk sensitivity of $S_\mathrm{d} = 0.09\,\mathrm{eRIU/RIU}$, where eRIU stands for effective refractive index units. We additionally computed the differential surface sensitivity of the waveguide by calculating the change in the effective index of the guided modes as a function of the thickness of a biorecognition layer with a refractive index of 1.45 RIU attached to the waveguide surface [30], [31], obtaining a value of $3.67\ \ 10^{\ 5}\,\mathrm{eRIU/nm}$. The impact of thermal fluctuations has also been studied theoretically. Our sensing waveguide exhibits a simulated sensitivity to temperature changes of $1.14\ \ 10^{\ 5}\,\mathrm{eRIU/\ C}$, which is two times lower than the $2.3\ 10^{\ 5}\,\mathrm{eRIU/\ C}$ obtained for a conventional single-mode MZI designed for the same platform. To maintain a compact layout while increasing overall sensitivity, we chose a spiralled waveguide [see Fig. 3] with a length of $7.81\,\mathrm{mm}$, thus yielding an overall bulk sensitivity of $S_\mathrm{bulk} = 2.85\ \ 10^3\,\mathrm{rad/RIU}$ and a surface sensitivity $S_\mathrm{surf} = 1.16\,\mathrm{rad/nm}$. This length is close to the optimum length of $9\,\mathrm{mm}$ estimated by evaluating the loss induced by the water-based sample at the design wavelength [32]. Our spirals follow the pattern proposed in [33]. The bend radius is kept at high values, i.e. over $240\ \ \mathrm{m}$, for the majority of the spiral path. Smaller radii are reached just at the vicinity of the center of the spiral, with a minimum of $86.6\ \ \mathrm{m}$. We computed a total radiation loss of 0.06 dB for the first high-order mode by integrating the mode attenuation constant, which varies with the changing radius, along the spiral path. As we will discuss in section IV, even if the waveguides were narrower (due to over-etching) the radiation losses would remain acceptable. Finally, a $35\ \ \mathrm{m}$ distance between adjacent waveguides was selected to avoid coupling. With these parameters the area occupied by the spiral is just $0.72\,\mathrm{mm}^2$.

IV. Experimental results

The experimental setup employed in this work is schematized in Fig. 3. The input signal generated by a laser source (Santec TSL-770) operating at a fixed wavelength of $1550\,\mathrm{nm}$ is amplified with an erbium-doped fiber amplifier (EDFA) (IPG Photonics EAD-500-C) and coupled into the chip with an angled-polished fiber array (O/E Land) via grating couplers. Polarization is optimized with a manual polarization controller (Thorlabs FPC562). After light propagation through the chip, the three output signals of the sensor are out-coupled to the fiber array and carried to three amplified photodetectors (Thorlabs PDA10CS2). The detected signals are then digitalized by a 24 bit DAQ module (NI 9239) and further processed with an in-house Matlab code to perform the calibration and phase extraction [22]. A custom PDMS microfluidic flow-cell and a methacrylate holder were designed to assure both complete coverage of the sensing spiral and hermetical sealing.

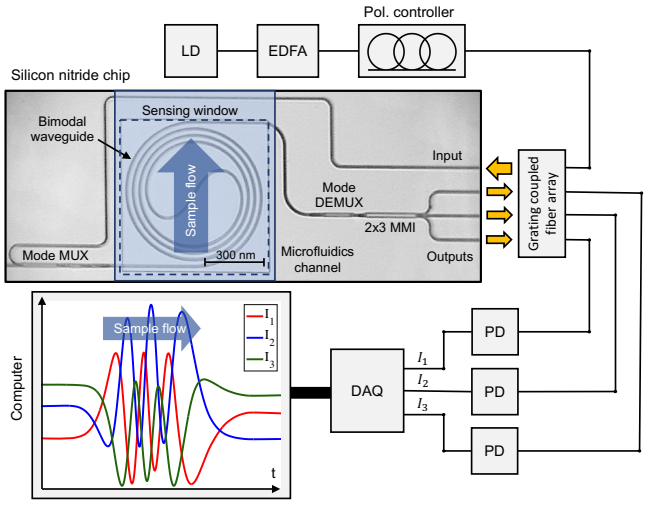

Fig. 3. Schematic representation of the measurement setup. The input signal is generated by a laser (LD), amplified by an EDFA and carried through a polarization controller into a fiber array. Coupling to and from the chip is performed via grating couplers. The three output signals are photodetected (PD), digitalized (DAQ) and processed with Matlab. A fragment of the detected intensity signals in a bulk sensing experiment is shown. A withdrawal pump is employed to flow the samples through a PDMS channel placed on top of the sensing area of the chip.

Four solutions of sodium chloride (NaCl) diluted in de-ionized, purified water (MilliQ) with concentrations of 1.5w%, 3w%, 6w% and 12w%, where w% expresses weight-percentage, were prepared. The refractive index of each sample was calculated following the model from [34]. These samples were flowed through the microfluidic channel by means of a withdrawal pump (New Era NE-1000) set at a constant rate of $30\ \ \mathrm{L/min}$. Figure 4(a) shows the retrieved phase after acquisition, digital low-pass filtering with a bandwidth of $1\,\mathrm{Hz}$, complex signal generation and calibration. Fig.4(b) shows the saturation values of the phase signal as a function of the change in refractive index between the samples. A linear fit yields an overall bulk sensitivity of $3.69\ \ 10^3\,\mathrm{rad/RIU}$. This result slightly exceeds the theoretical sensitivity calculated in section III. This can be explained by an over-etching of

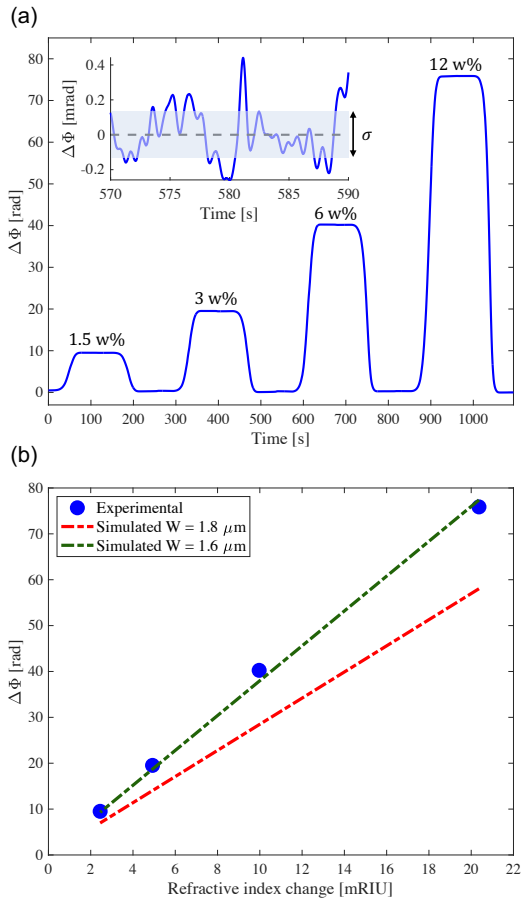

Fig. 4. (a) Detected phase signal in a bulk sensing experiment with different solutions of NaCl in water. A sensitivity of 3.69 10^3 rad/RIU and a LOD of 1.67 10^{-7} RIU were obtained. A typical noise fragment is shown in the inset. (b) Experimental saturation phase-shift as a function of the refractive index change of the cladding and its simulated values for different widths of the bimodal waveguide. Our results agree with a 1.6 m width.

the sensing waveguide during the fabrication process, which would lead to a narrower waveguide and, therefore, a higher differential sensitivity. Indeed, the over-etching is expected to be higher in the sensing region than in the rest of the chip, as a result of unintended additional etching during the cladding removal to create the sensing window. As shown in Fig. 4(b), our experimental results closely match those obtained by simulating a bimodal waveguide with a width of 1.6 m, which would reach a differential mode sensitivity $S_{\mathrm{d}} = 0.12\,\mathrm{eRIU/RIU}$. The total radiation loss for the first high-order mode would amount to 7 dB in this scenario. The fact that all the elements of the sensor work well and our signal-to-noise ratio is over 50 dB despite these fabrication deviations further highlights the robustness of our sensing architecture.

To determine the 3σ limit of detection, the standard deviation of a 20 second fragment of the sensor baseline [see inset in Fig. 4(a)] was evaluated. We obtained a phase noise of $0.14\,\mathrm{mrad}$, yielding a LOD $= 3\sigma/S_{\mathrm{bulk}} = 1.67$ 10 ^{7} RIU. As shown in Table II, this value is among the best reported in literature for bimodal waveguides. This result is remarkable taking into account that the waveguide only provides a moderate sensitivity, and that water absorption is strong at the operating wavelength. We attribute this to both well optimized optical circuitry and low noise in the coherent readout.

V. Conclusions

We have experimentally shown that by combining a bimodal waveguide with robust on-chip mode (de)multiplexing and coherent phase read-out, compact and high-performance interferometric sensors can be implemented. Our design has a reduced footprint, can be readily fabricated with standard silicon-nitride foundry processes, and achieves state-of-the-art detection limits of the order of 10 ^{7} RIU. We therefore believe that our sensors, when combined with adequate surface functionalization, are ideally suited for the detection of analytes in very low concentrations.

Acknowledgement

This work has received funding from the Ministerio de Universidades, Ciencia e Innovación (FPU19/03330, PID2019-106747RB-I00, PID2020-115204RB-I00), the Junta de Andalucía (Agencia Andaluza del Conocimiento PY18-793, Consejería de salud y familia PIN-0113-2020), and project TED2021-130400B-I00/ AEI/10.13039/501100011033/ Unión Europea NextGenerationEU/PRTR.

References

[1] N. L. Kazanskiy, S. N. Khonina, and M. A. Butt, "Advancement in silicon integrated photonics technologies for sensing applications in near-infrared and mid-infrared region: A review," *Photonics*, vol. 9, no. 5, 2022.

[2] A. Grosman, T. Duanis-Assaf, N. Mazurski, R. Zektzer, C. Frydendahl, L. Stern, M. Reches, and U. Levy, "On-chip multivariant COVID 19 photonic sensor based on silicon nitride double-microring resonators," *Nanophotonics*, 2023.

[3] H. D. Yallew, M. Vlk, A. Datta, S. Alberti, J. Høvik, A. Aksnes, M. M. Greve, and J. Jágerská, "Silicon-on-insulator (SOI) slot waveguide for methane absorption sensing in the mid-infrared," in *Optical Sensors and Sensing Congress 2022 (AIS, LACSEA, Sensors, ES)*, p. EM1D.2, Optica Publishing Group, 2022.

[4] M. Estevez, M. Alvarez, and L. Lechuga, "Integrated optical devices for lab-on-a-chip biosensing applications," *Laser & Photonics Reviews*, vol. 6, no. 4, pp. 463–487, 2012.

[5] S. Hassan, C. C. Schreib, X. Zhao, G. Duret, D. S. Roman, V. Nair, T. Cohen-Karni, O. Veiseh, and J. T. Robinson, "Real-time in vivo sensing of nitric oxide using photonic microring resonators," *ACS Sensors*, vol. 7, no. 8, pp. 2253–2261, 2022.

[6] R. Armand, M. Perestjuk, A. Della Torre, M. Sinobad, A. Mitchell, A. Boes, J.-M. Hartmann, J.-M. Fedeli, V. Reboud, P. Brianceau, A. De Rossi, S. Combrié, C. Monat, and C. Grillet, "Mid-infrared integrated silicon–germanium ring resonator with high Q-factor," *APL Photonics*, vol. 8, no. 7, p. 071301, 2023.

[7] F. Vogelbacher, T. Kothe, P. Muellner, E. Melnik, M. Sagmeister, J. Kraft, and R. Hainberger, "Waveguide mach-zehnder biosensor with laser diode pumped integrated single-mode silicon nitride organic hybrid solid-state laser," *Biosensors and Bioelectronics*, vol. 197, p. 113816, 2022.

[8] H. Niu, P. Yu, Y. Zhu, Z. Jing, P. Li, B. Wang, C. Ma, J. Wang, J. Wu, A. O. Govorov, A. Neogi, and Z. M. Wang, "Mach-Zehnder interferometer based integrated-photonic acetone sensor approaching the sub-ppm level detection limit," *Optics Express*, vol. 30, no. 16, pp. 29665–29679, 2022.

[9] G. Besselink, A. Schütz-Trilling, J. Veerbeek, M. Verbruggen, A. van der Meer, R. Schonenberg, H. Dam, K. Evers, E. Lindhout, A. Garritsen, A. van Amerongen, W. Knoben, and L. Scheres, "Asymmetric Mach-Zehnder interferometric biosensing for quantitative and sensitive multiplex detection of anti-sars-cov-2 antibodies in human plasma," *Biosensors*, vol. 12, no. 8, 2022.

TABLE II
COMPARISON OF DIFFERENT BIMODAL WAVEGUIDE SENSORS. N.D. STANDS FOR NOT DETERMINED BY THE AUTHORS.

Configuration	Platform	Wavelength	Modal splitter	Readout technique	Bulk sensitivity	LOD	Ref.
Spiral BI	SOI	1550 nm	Horizontal	Conventional	$1.45\ 10^3$ rad/RIU	$2.2\ 10^{-5}$ RIU	[13]
Vertical BI	Si_3N_4	633 nm	Vertical	Conventional	$1.3\ 10^4$ rad/RIU	$5\ 10^{-8}$ RIU	[35]
Vertical BI	Si_3N_4	600 nm	Vertical	Phase modulation and trigonometric algorithm	$1.7\ 10^4$ rad/RIU	$3.21\ 10^{-7}$ RIU	[14]
SWG BI	SOI	1550 nm	Horizontal	Swept wavelength	2270 nm/RIU	$2\ 10^{-5}$ RIU	[15]
Slow light BI	SOI	1550 nm	Horizontal	Swept wavelength	0.52 rad/RIU	$6.6\ 10^{-6}$ RIU	[16]
Grating BI	SOI	1550 nm	Mode filter	Swept wavelength	1600 nm/RIU[a]	N.D.	[18]
Coherent BI	SOI	1544 nm	Mode converter	Coherent detection	$8\ 10^3$ rad/RIU[b]	N.D.	[36]
Coherent BI	Si_3N_4	1550 nm	Mode converter	Coherent detection	$3.69\ 10^3$ rad/RIU	$1.67\ 10^{-7}$ RIU	This work

[a] Value obtained from numerical simulations.
[b] Value estimated from wavelength sweep measurements.

[10] J. Leuermann, V. Stamenkovic, P. Ramirez-Priego, A. Sánchez-Postigo, A. Fernández-Gavela, C. A. Chapman, R. C. Bailey, L. M. Lechuga, E. Perez-Inestrosa, D. Collado, R. Halir, and I. Molina-Fernández, "Coherent silicon photonic interferometric biosensor with an inexpensive laser source for sensitive label-free immunoassays," *Optics Letters*, vol. 45, no. 24, pp. 6595–6598, 2020.

[11] K. E. Zinoviev, A. B. González-Guerrero, C. Domínguez, and L. M. Lechuga, "Integrated bimodal waveguide interferometric biosensor for label-free analysis," *Journal of Lightwave Technoly*, vol. 29, no. 13, pp. 1926–1930, 2011.

[12] J. Maldonado, A. B. González-Guerrero, A. Fernández-Gavela, J. J. González-López, and L. M. Lechuga, "Ultrasensitive label-free detection of unamplified multidrug-resistance bacteria genes with a bimodal waveguide interferometric biosensor," *Diagnostics*, vol. 10, no. 10, 2020.

[13] Q. Liu, K. W. Kim, Z. Gu, J. S. Kee, and M. K. Park, "Single-channel Mach-Zehnder interferometric biochemical sensor based on two-lateral-mode spiral waveguide," *Optics Express*, vol. 22, no. 23, pp. 27910–27920, 2014.

[14] B. Bassols-Cornudella, P. Ramirez-Priego, M. Soler, M.-C. Estévez, H. J. D. Luis-Ravelo, M. Cardenosa-Rubio, and L. M. Lechuga, "Novel sensing algorithm for linear read-out of bimodal waveguide interferometric biosensors," *Journal of Lightwave Technoly*, vol. 40, no. 1, pp. 237–244, 2022.

[15] L. Torrijos-Morán, A. Griol, and J. García-Rupérez, "Experimental study of subwavelength grating bimodal waveguides as ultrasensitive interferometric sensors," *Optics Letters*, vol. 44, no. 19, pp. 4702–4705, 2019.

[16] L. Torrijos-Morán, A. Griol, and J. García-Rupérez, "Slow light bimodal interferometry in one-dimensional photonic crystal waveguides," *Light: Science & Applications*, vol. 10, p. 16, 2021.

[17] R. Bruck and R. Hainberger, "Sensitivity and design of grating-assisted bimodal interferometers for integrated optical biosensing," *Optics Express*, vol. 22, no. 26, pp. 32344–32352, 2014.

[18] A. Tsarev, "Design of the bimodal grating sensor with a built-in mode demultiplexer," *Sensors*, vol. 23, no. 9, 2023.

[19] S. Dante, D. Duval, D. Fariña, A. B. González-Guerrero, and L. M. Lechuga, "Linear readout of integrated interferometric biosensors using a periodic wavelength modulation," *Laser & Photonics Reviews*, vol. 9, no. 2, pp. 248–255, 2015.

[20] Y. E. Marin, V. Toccafondo, P. Velha, S. Scarano, S. Tirelli, A. Nottola, Y. Jeong, H. Jeon, S. Kim, M. Minunni, F. Di Pasquale, and C. J. Oton, "Silicon photonic biochemical sensor on chip based on interferometry and phase-generated-carrier demodulation," *IEEE Journal of Selected Topics in Quantum Electronics*, vol. 25, no. 1, pp. 1–9, 2019.

[21] C. Schweikert, N. Hoppe, W. Vogel, and M. Berroth, "120° hybrid for bimodal interferometers," in *2022 International Conference on Numerical Simulation of Optoelectronic Devices (NUSOD)*, pp. 179–180, 2022.

[22] R. Halir, L. Vivien, X. Le Roux, D.-X. Xu, and P. Cheben, "Direct and sensitive phase readout for integrated waveguide sensors," *IEEE Photonics Journal*, vol. 5, no. 4, p. 6800906, 2013.

[23] L. Torrijos-Morán, B. D. Lisboa, M. Soler, L. M. Lechuga, and J. García-Rupérez, "Integrated optical bimodal waveguide biosensors: Principles and applications," *Results in Optics*, vol. 9, p. 100285, 2022.

[24] D. González-Andrade, J. G. Wangüemert-Pérez, A. Velasco-Villafranca, A. Ortega-Moñux, A. Herrero-Bermello, I. Molina-Fernández, R. Halir, and P. Cheben, "Ultra-broadband mode converter and multiplexer based on sub-wavelength structures," *IEEE Photonics Journal*, vol. 10, no. 2, pp. 1–10, 2018.

[25] D. González-Andrade, A. Dias, J. G. Wangüemert-Pérez, A. Ortega-Moñux, Íñigo Molina-Fernández, R. Halir, P. Cheben, and A. Villafranca-Velasco, "Experimental demonstration of a broadband mode converter and multiplexer based on subwavelength grating waveguides," *Optics & Laser Technology*, vol. 129, p. 106297, 2020.

[26] P. J. Reyes-Iglesias, I. Molina-Fernández, A. Moscoso-Mártir, and A. O.-M. nux, "High-performance monolithically integrated 120° downconverter with relaxed hardware constraints," *Optics Express*, vol. 20, no. 5, pp. 5725–5741, 2012.

[27] "Cornerstone project." https://www.cornerstone.sotonfab.co.uk.

[28] "Rsoft photonic device tools." https://www.synopsys.com/photonic-solutions/rsoft-photonic-device-tools.html.

[29] L. Soldano and E. Pennings, "Optical multi-mode interference devices based on self-imaging: principles and applications," *Journal of Lightwave Technology*, vol. 13, no. 4, pp. 615–627, 1995.

[30] K. D. Vos, I. Bartolozzi, E. Schacht, P. Bienstman, and R. Baets, "Silicon-on-insulator microring resonator for sensitive and label-free biosensing," *Optics Express*, vol. 15, no. 12, pp. 7610–7615, 2007.

[31] J. Vörös, "The density and refractive index of adsorbing protein layers," *Biophysical Journal*, vol. 87, no. 1, pp. 553–561, 2004.

[32] I. Molina-Fernández, J. Leuermann, A. Ortega-Moñux, J. G. Wangüemert-Pérez, and R. Halir, "Fundamental limit of detection of photonic biosensors with coherent phase read-out," *Optics Express*, vol. 27, no. 9, pp. 12616–12629, 2019.

[33] A. D. Simard, Y. Painchaud, and S. LaRochelle, "Integrated bragg gratings in spiral waveguides," *Optics Express*, vol. 21, no. 7, pp. 8953–8963, 2013.

[34] J. E. Saunders, C. Sanders, H. Chen, and H.-P. Loock, "Refractive indices of common solvents and solutions at 1550 nm," *Applied Optics*, vol. 55, no. 4, pp. 947–953, 2016.

[35] A. B. González-Guerrero, J. Maldonado, S. Dante, D. Grajales, and L. M. Lechuga, "Direct and label-free detection of the human growth hormone in urine by an ultrasensitive bimodal waveguide biosensor," *Journal of Biophotonics*, vol. 10, no. 1, pp. 61–67, 2017.

[36] C. Schweikert, A. Tsianaka, N. Hoppe, R. H. Klenk, R. Elster, M. Greul, M. Kaschel, A. Southan, W. Vogel, and M. Berroth, "Integrated polarization mode interferometer in 220-nm silicon-on-insulator technology," *Optics Letters*, vol. 47, no. 17, pp. 4536–4539, 2022.